Article ID: 1000-7032(2025)06-1037-11

Ultrafast Self-powered Near-infrared Photodetectors and Imaging Array Based on Tin-lead Mixed Perovskites

LIU Jingjing[1,2], YANG Zhichun[1,2*], BAO Haotian[1,2], MENG Xinqin[1,2], QI Minru[1,2], YANG Changgang[1,2], ZHANG Guofeng[1,2], QIN Chengbing[1,2*], XIAO Liantuan[1,2*], JIA Suotang[1,2]

(1. *State Key Laboratory of Quantum Optics Technologies and Devices, Institute of Laser Spectroscopy, Shanxi University, Taiyuan* 030006, *China*;
2. *Collaborative Innovation Center of Extreme Optics, Shanxi University, Taiyuan* 030006, *China*)

* *Corresponding Authors, E-mail: yangzhichun@sxu. edu. cn; chbqin@sxu. edu. cn; xlt@sxu. edu. cn*

Abstract: Tin-lead (Sn-Pb) mixed perovskites are extensively investigated in near-infrared (NIR) photodetectors (PDs) owing to their excellent photoelectric performance. However, achieving high-performance Sn-Pb mixed PDs remains challenging, primarily because of the rapid crystallization and the susceptibility of Sn^{2+} to oxidation. To address these issues, this study introduces the multifunctional molecules 2,3-difluorobenzenamine (DBM) to modulate the crystallization of Sn-Pb mixed perovskites and retard the oxidation of Sn^{2+}, thereby significantly enhancing film quality. Compared with the pristine film, Sn-Pb mixed perovskite films modulated by DBM molecules exhibit a highly homogeneous morphology, reduced roughness and defect density. The self-powered NIR PDs fabricated with the improved films have a spectral response range from 300 nm to 1 100 nm, a peak responsivity of 0.51 $A\cdot W^{-1}$, a specific detectivity as high as 2.46×10^{11} Jones within the NIR region (780 nm to 1 100 nm), a linear dynamic range exceeding 152 dB, and ultrafast rise/fall time of 123/464 ns. Thanks to the outstanding performance of PDs, the fabricated 5 × 5 PDs array demonstrates superior imaging ability in the NIR region up to 980 nm. This work advances the development of Sn-Pb mixed perovskites for NIR detection and paves the way for their commercialization.

Key words: tin-lead mixed perovskites; near-infrared photodetectors; imaging array; oxidation; crystallization modulation
CLC number: O482.31 **Document code**: A
DOI: 10.37188/CJL.20250027 **CSTR**: 32170.14.CJL.20250027

基于锡铅混合钙钛矿的超快自驱动近红外光电探测器与成像阵列

刘晶晶[1,2], 杨志春[1,2*], 包昊天[1,2], 孟新钦[1,2], 齐敏如[1,2], 杨昌钢[1,2], 张国峰[1,2], 秦成兵[1,2*], 肖连团[1,2*], 贾锁堂[1,2]

(1. 山西大学 激光光谱研究所, 光量子技术与器件全国重点实验室, 山西 太原 030006;
2. 山西大学 极端光学协同创新中心, 山西 太原 030006)

摘要: 锡铅(Sn-Pb)混合钙钛矿因其卓越的光电特性,在近红外光电探测器领域得以快速发展。然而,由于其

收稿日期: 2025-02-07; **修订日期**: 2025-02-20
基金项目: 国家重点研发计划(2022YFA1404201); 国家自然科学基金(62205187, U23A20380, U22A2091, 62222509, 62127817, 62075120); 教育部长江学者和创新团队发展计划(IRT_17R70); 山西省基础研究计划(202103021223032, 202303021222031); 中国博士后科学基金(2022M722006); 山西省"1331工程"重点学科建设计划
Supported by National Key Research and Development Program of China(2022YFA1404201); National Natural Science Foundation of China(62205187, U23A20380, U22A2091, 62222509, 62127817, 62075120); Changjiang Scholars and Innovative Research Team in University of Ministry of Education of China (IRT_17R70); Fundamental Research Program of Shanxi Province(202103021223032, 202303021222031); Project Funded by China Postdoctoral Science Foundation(2022M722006); Fund for Shanxi "1331 Project" Key Subjects Construction

固有的快速结晶特性和Sn^{2+}易氧化的问题，实现高性能锡铅混合光电探测器仍面临巨大挑战。为了解决这一问题，该研究引入了多功能分子2,3-二氟苯胺(DBM)，以调控Sn-Pb混合钙钛矿的结晶过程并且延缓Sn^{2+}氧化，从而有效提升薄膜质量。与原始薄膜相比，经DBM分子调控的Sn-Pb混合钙钛矿薄膜具有高度均匀的形貌、显著降低的粗糙度和缺陷密度。基于这种调控薄膜制备的自驱动型近红外光电探测器，光谱响应范围为300~1 100 nm，最高响应度为0.51 $A\cdot W^{-1}$，近红外区域(780~1 100 nm)的比探测率高达2.46×10^{11} Jones，线性动态范围超过152 dB，响应时间为123/464 ns。在此基础上制备的5×5光电探测器阵列在近红外区域(最高可达980 nm)展现了卓越的成像能力。该工作不仅促进了Sn-Pb混合钙钛矿在近红外探测与成像领域的快速发展，还为其商业化进程奠定了基础。

关 键 词：锡铅混合钙钛矿；近红外光电探测器；成像阵列；氧化；结晶调控

1 Introduction

Near-infrared(NIR) photodetectors(PDs) have been extensively utilized in the domains of environmental monitoring, remote sensing, security monitoring, space exploration, night vision, optical communications, autonomous driving and bioimaging[1-3]. The current commercial NIR PDs are primarily fabricated from traditional inorganic materials like silicon, germanium, and indium gallium arsenide. However, the inherent shortcomings of these materials, such as high production cost, complex manufacturing process, and the need for an external bias voltage, limit their further applications[4]. Therefore, it is urgent to develop new alternative semiconductor materials to break through these limitations. Metal halide perovskite has the advantages of high optical absorption coefficient, tunable bandgap, high carrier mobility, abundant material source, low cost, solution processing *etc.*, which make it a competitive candidate in the next generation of semiconductors[5-7]. Pb-based perovskites represent the most extensively investigated subgroup within the family of metal halide perovskites. However, the relatively large bandgap (~1.45 eV) limits their spectral response to a range up to 850 nm, restricting their applications in NIR imaging. Additionally, the presence of Pb poses significant environmental and health risks[8]. Although non-toxic pure Sn-based perovskites can broaden the response range and enhance environmental friendliness, they are not an ideal solution due to their poor stability and high defect density, which result from the oxidation of Sn^{2+}. In recent years, tin-lead (Sn-Pb) mixed perovskites have developed rapidly as an effective solution[9-10]. Due to the advantages of both pure Sn-based and Pb-based perovskites, Sn-Pb mixed perovskites extend the spectral response range, environmental friendliness and stability. More importantly, because the ionic radii of Sn^{2+} and Pb^{2+} are similar and their atomic structures are comparable, replacing part of the Pb with Sn can effectively preserve the original crystal structure of the perovskite, thereby avoiding issues related to structural damage[11].

However, owing to the following key challenges, the film quality and device performance of Sn-Pb mixed perovskites still fall short of the anticipated targets: (1) the extremely fast and uncontrolled crystallization leads to inferior film quality and device performance; (2) the oxidation of Sn^{2+} to Sn^{4+} increases the Sn vacancies in perovskite lattice, p-type self-doping, and trap-assisted non-radiative recombination. Researchers have proposed solvent engineering, additive engineering and cation engineering to regulate crystallization of Sn-Pb mixed perovskite films and introduced antioxidants into the prepared precursor solution to retard the oxidation of Sn^{2+}. Despite the tremendous efforts made to address the aforementioned issues, the inevitable Sn vacancies still limit the quality of Sn-Pb mixed perovskites. Recently, some representative multifunctional molecular strategies have been proposed to achieve superior Sn-Pb mixed perovskite films for high-performance optoelectronic devices. However, the low dark current density (J_d), high specific detectivity (D^*), and ultrafast response for the PDs are still impending steps to promote the practical scenario application of NIR

imaging based on Sn-Pb mixed perovskites.

In this work, the multifunctional molecule 2,3-difluorobenzenamine(DBM) is effectively introduced to slow down the oxidation and regulate the crystallization of Sn-Pb mixed perovskites. The optimal doped Sn-Pb mixed perovskite films exhibit homogeneous surface morphology, reduced roughness, and lower defect density compared to the pristine film, all of which contribute to excellent device performance. Based on the doped perovskite thin film, we further fabricated p-i-n self-powered NIR PDs. The optimal PDs achieve an impressive responsivity (R) of 0.51 A·W^{-1}, a D^* as high as 2.46 × 10^{11} Jones, a large linear dynamic range (LDR) of 152 dB, and ultrafast rise/fall time of 123/464 ns without an applied bias voltage, which represents an advanced level for Sn-Pb mixed perovskite NIR PDs. Finally, a 5×5-pixel imaging array is fabricated and demonstrates excellent NIR imaging performance.

2　Experiment

2.1　Sn-Pb Mixed Perovskites Precursor Preparation

1.1 mol·L^{-1} $FA_{0.7}MA_{0.3}Sn_{0.5}Pb_{0.5}I_3$ was prepared for the construction of PDs and the imaging array. Specifically, the precursors of FAI (0.132 4 g), MAI (0.052 4 g), SnI_2 (0.204 9 g), PbI_2 (0.253 6 g), Sn powder (0.002 5 g), SnF_2 (0.008 6 g) and DBM (0.002 3 g, 2% in relation to the molar ratio of $Pb_{0.5}Sn_{0.5}$) were dissolved into the mixed solvent of N,N-dimethylformamide (DMF) and dimethyl sulfoxide (DMSO) (volume ratio of 4∶1). The precursor solutions were stirred for 2 hours at ambient temperature. All solutions were filtered through a 0.22 μm membrane prior to use.

2.2　Devices Fabrication

Firstly, a nanosecond pulsed laser (355 nm, 3 W) was employed to scribe indium tin oxide (ITO) glass substrates. Subsequently, the etched ITO glass underwent a series of ultrasonic cleaning processes using detergent, deionized water, ethanol, acetone, and isopropanol for a total duration of 20 min. The washed ITO substrates were subsequently dried at 100 ℃ in an oven overnight. Prior to utilization, they should be further cleaned with the UV-ozone (UVO) for 20 min and subsequently sent into the glovebox (in a nitrogen atmosphere) for standby. Dissolve 2 mg of poly[bis(4-phenyl)(2,4,6-trimethylphenyl)amine (PTAA)] in 1 mL of toluene solution and spin-coated it onto a cleaned ITO substrate at 5 000 r·min^{-1} for 30 s. The coated substrate was then annealed at 100 ℃ for 10 min. Next, the perovskite precursor ink was applied to the PTAA layer using a two-step spin-coating process: first spun at 1 000 r·min^{-1} for 10 s, followed by spinning at 5 000 r·min^{-1} for 30 s. This film was then annealed at 100 ℃ for 10 min. Finally, under vacuum conditions below 5.0 × 10^{-4} Pa, C_{60}, bathocuproine (BCP), and Ag or Au electrodes were sequentially deposited *via* thermal evaporation. The evaporation rate was maintained at 0.01 nm·s^{-1} with thicknesses of 28 nm for C_{60}, 6 nm for BCP, and 100 nm for the metal electrode.

3　Results and Discussion

We term the samples without the DBM molecules are referred to as "Pristine", and the samples containing DBM molecules as "DBM". We investigated the interaction mechanism between DBM molecules and perovskite precursor solutions and their effects on the quality of perovskite films and device properties. As shown in Fig. S1, the -NH_2 group can interact with organic cations in the perovskite precursor solution *via* hydrogen bonding, which reduces ion residues, adjusts crystal orientation, and effectively retards the crystallization. This interaction can passivate film defects, ultimately enhancing perovskite films quality. Meanwhile, due to the electron absorption effect of the phenyl group, the electrostatic potential on the N atom directly attached to the benzene ring becomes more positive, which leads to more efficient defect passivation[12-14]. The DBM molecules possess a -NH_2 functional group and the N atom is directly connected to the phenyl group. Thus, it can effectively regulate the film crystallization and reduce defects. The electrostatic potential of the DBM molecules is shown in Fig. 1(a), is dominated by the positive potential (blue area), indicating a

strong electron absorption ability[15-16]. Next, a comparative analysis was conducted on the natural crystallization of perovskite intermediate films with and without the presence of DBM to explore the influence of DBM molecules on the crystallization of Sn-Pb mixed perovskite, the result is shown in Fig. S2. Under the same preparation conditions, the transformation of DBM-perovskite films from reddish-brown to black is conspicuously retarded, indicating a significantly slowed crystallization process. This demonstrates DBM's efficacy in retarding crystallization[17]. Relevant videos are shown in the Video S1.

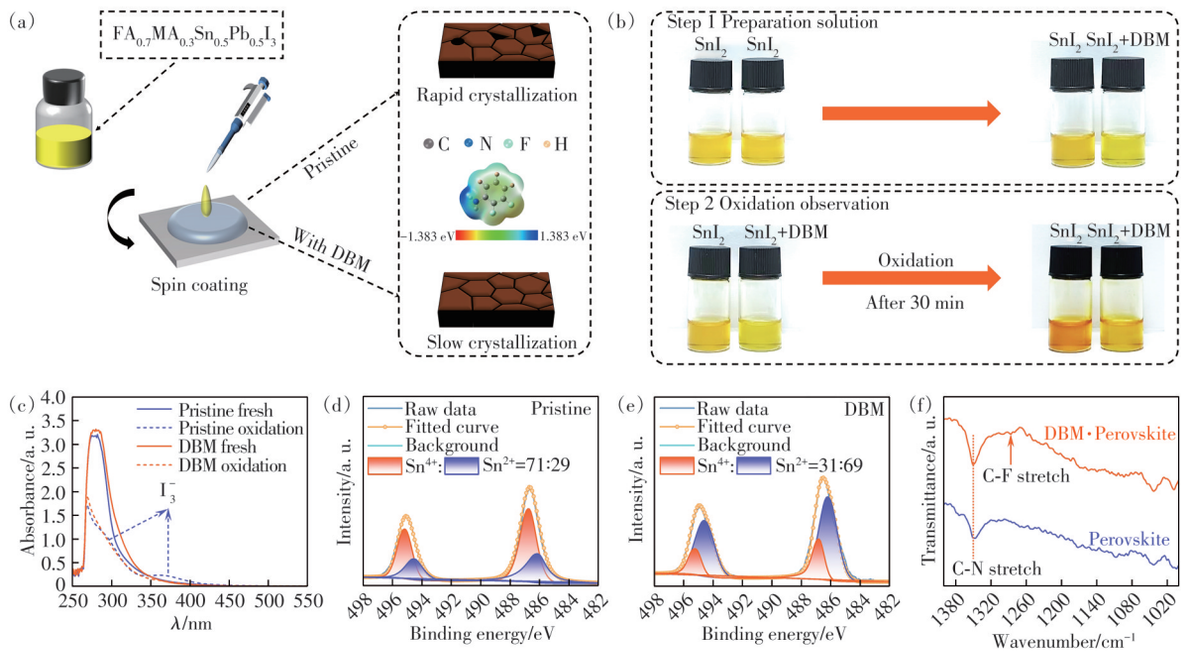

Fig. 1 (a) The influence of DBM molecules on the microstructure evolution of perovskite films. (b) Oxidation of SnI_2 solution without and with DBM. (c) *In-situ* UV-Vis absorption spectra of 1 mmol·L^{-1} SnI_2 solutions. (d)-(e) XPS spectra of Sn 3d for pristine and DBM-perovskite films. (f) FTIR results of pristine and DBM-perovskite films

To study the retarded oxidation process of Sn^{2+} by the DBM molecules, SnI_2 powders were separately dissolved in DMF without and with DBM molecules at the concentration of 1 mol·L^{-1} in glovebox. Subsequently, the DBM molecules were added to one bottle of the solutions to form the experimental group. A rapid color change was observed in the SnI_2 solution while introducing the DBM molecules, as shown at the top of Fig. 1(b) and top right corner of Video S2. Following this, both bottles of solution were removed from the glovebox, and their oxidation states were observed at room temperature. The solution containing the DBM molecules exhibits lighter color changes after being exposed to O_2 for 30 min. In contrast, the solution without the DBM molecules demonstrates a brown color, signifying the oxidation of Sn^{2+}[18-20]. It is evident that the presence of the DBM molecules effectively retards the oxidation process of Sn^{2+}, as demonstrated in the Video S2. Furthermore, this observation is supported by *in-situ* UV-Vis absorption spectra analysis conducted on SnI_2 solutions dissolved in DMF, with and without DBM at a concentration of 1 mmol·L^{-1}, respectively. As shown in Fig. 1(c) and Fig. S3, the pristine Sn^{2+} solution exhibited two significant absorption peaks at 293 nm and 365 nm after being exposed to indoor conditions for over 40 min. These peaks are attributed to the generation of I_3^-. In contrast, even after more than 50 min of exposure to the DBM-modulated SnI_2 solution, no absorption peak corresponding to I_3^- generation was detected. Generally, the oxidation degree of Sn^{2+} can be evaluated by the oxidation of I^- to I_3^-, due to the oxidation of Sn^{2+} occurs prior to that of I^- ($Sn^{2+} \rightleftharpoons Sn^{4+} + 2e^-$, $3I^- \rightleftharpoons I_3^- + 2e^-$)[21]. Beyond that, the Sn^{2+} content in Sn-Pb mixed perovskite films was further analyzed using X-ray photoelectron spectroscopy (XPS). XPS analysis reveals that the content of Sn^{4+} in the DBM perovskite film is conspicuously

lower than that of the pristine sample (Fig. 1(d) and Fig. 1(e)), suggesting that the DBM molecules effectively restrain the oxidation of Sn^{2+}. Moreover, the UPS results (Fig. S4) indicate that the work function drops from 4.92 eV to 4.62 eV, further substantiating this conclusion. To reveal the mechanisms of the modulated crystallization of Sn-Pb mixed perovskites and the suppressed oxidation of Sn^{2+}, Fourier transform infrared spectroscopy (FTIR) and XPS were subsequently carried out. As depicted in Fig. 1(f), the C-F peak was detected in the DBM perovskite powder, and the vibration of the C-N bond was intensified. Concurrently, the N-H stretching vibration peaks in FAI-DBM and MAI-DBM shifted conspicuously to lower wavenumbers (Fig. S5), signifying the strong interactions between DBM molecules and perovskite precursors[22-24]. The binding energy shifts of Sn 3d, Pb 4f, I 3d, and N 1s in XPS result further substantiated this interaction. Furthermore, the characteristic peak of the fluorine element was identified in the perovskite films with the addition of DBM, suggesting that DBM molecules remained in the final films (Fig. S6).

Firstly, the surface morphology of the films was analyzed by scanning electron microscopy (SEM) and the impact of DBM molecules on the morphology of Sn-Pb mixed perovskite films was revealed. As exhibited in Fig. 2(a), the pristine film contained several pinholes while the DBM-perovskite film showed compact surface morphology. This improvement facilitates carrier transport and enhances device performance[25]. This result is also confirmed by the cross-sectional SEM images of perovskite films with or without DBM molecules (Fig. S7). Furthermore, the defect state density was quantitatively assessed by the space charge limited current method. The outcome indicates that DBM conspicuously reduces the defect state density (Fig. S8) in both hole-only and electron-only devices. To evaluate the crystallinity of the as-prepared perovskite films, we performed X-ray diffraction (XRD) measurements. As exhibited in Fig. 2(b), the peak intensities corresponding to (100) and (200) planes in the XRD results are significantly enhanced for the DBM-perovskite film compared to the pristine sample, indicating an improvement in the film crystallinity.

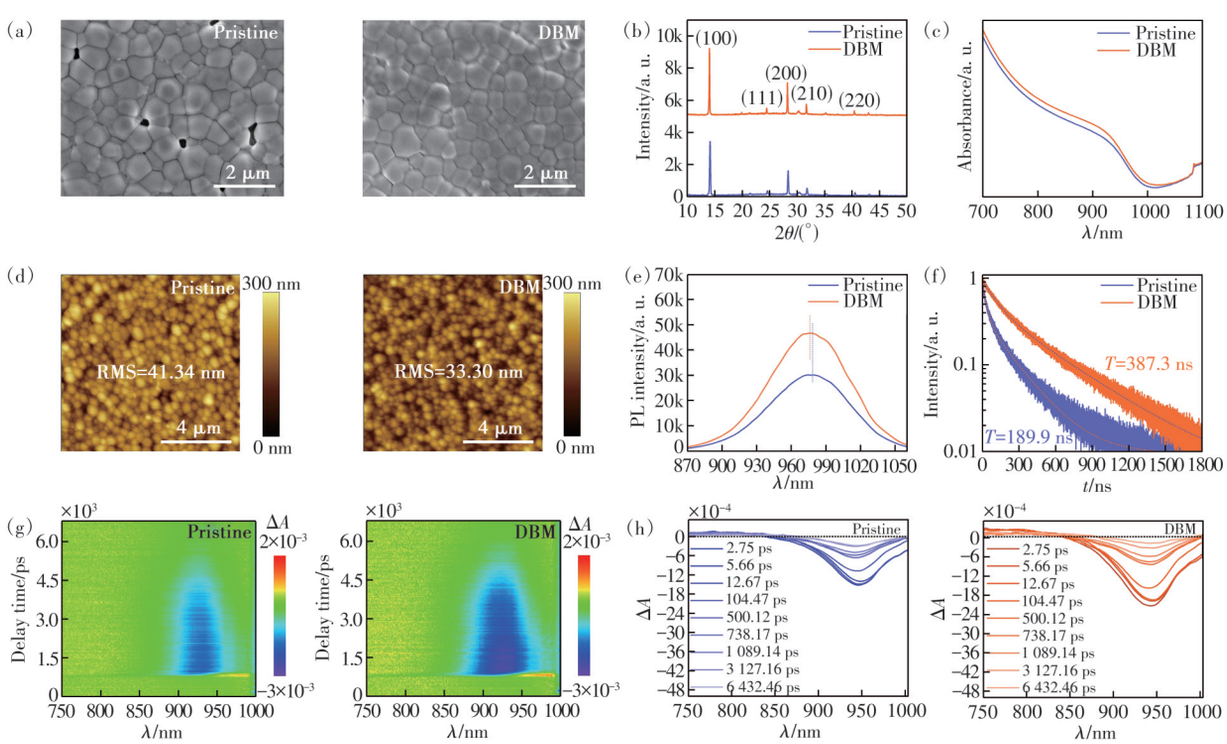

Fig. 2　Top-view SEM images(a), XRD(b), UV-Vis spectra(c), AFM images(d), PL spectra(e), TRPL spectra(f), 2D pseudocolor map of the transient absorption spectroscopy(g) and TAS curves(h) at different probe retards for the pristine and DBM-perovskite films

The improved film crystallinity can be ascribed to the regulated crystallization[26-27]. At the same time, the light-harvesting capacity and optical bandgap of the fabricated perovskite films were characterized using UV-Vis-NIR absorption spectroscopy. As shown in Fig. 2(c), the DBM-perovskite film exhibits enhanced light absorption in 700-1 000 nm compared to the pristine sample, which is attributed to its enhanced crystallinity[28]. Moreover, the Tauc plots reveal that the bandgaps of both samples are approximately 1.26 eV. This characteristic is favorable for the response of the prepared PDs to NIR light, as illustrated in Fig. S9. It is widely acknowledged that a favorable interface contact between the perovskite light-harvesting layer and the adjacent charge transport layer is conducive to facilitating carrier transport. Consequently, in this research, atomic force microscopy (AFM) was used to characterize the surface roughness of the perovskite films. The root-mean-square(RMS) roughness of the DBM-perovskite film is 33.30 nm, significantly lower than the 41.34 nm observed for the pristine film, indicating a relatively smooth and flat surface morphology (Fig. 2(d))[29]. Subsequently, crucial characterization techniques including steady-state photoluminescence(PL), time-resolved photoluminescence (TRPL), and femtosecond transient absorption spectroscopy (TAS) were adopted to systematically explore the carrier dynamics in perovskite films. As demonstrated in Fig. 2(e), compared to the pristine sample, the DBM-perovskite film exhibits a higher PL intensity. Furthermore, a notable blueshift (~2 nm) has been observed for the target film compared to the pristine sample, indicating the suppression of defect-assisted charge nonradiative recombination within the DBM-perovskite film. As exhibited in Fig. 2(f), the DBM-perovskite film exhibited a longer PL decay lifetime (387.3 ns, Tab. S1) than the pristine perovskite film (189.9 ns). The prolonged average carrier lifetime further confirms the suppressed charge nonradiative recombination loss in the DBM-perovskite film[30]. The TAS measurements of perovskite films were conducted using a pump excitation wavelength of 515 nm, with probing performed over a range from 700 nm to 1 000 nm. As shown in Fig. 2(g), the DBM-perovskite film showed a stronger ground-state bleaching (GSB) signal near 940 nm compared to the pristine sample. The generation of GSB signals is primarily ascribed to the sample's absorption of pump light and subsequent transition to the excited state, which leads to a reduction in the number of ground-state particles. It can be observed from the TAS of the pristine and the DBM-perovskite films at various time delays after pump excitation (Fig. 2(h)) that the decay rate of the latter slows down, suggesting a longer carrier lifetime and suppressed carrier recombination[31].

The high-quality perovskite film, regulated by the DBM molecules, exhibits low defect density, high crystallinity, appropriate energy levels, and strong NIR light absorption, making it promising for NIR optoelectronic device applications. Therefore, the device structure of the fabricated self-powered NIR PDs is ITO/PTAA/Sn-Pb mixed perovskite/C_{60}/BCP/Ag(Fig. 3(a)). Furthermore, some critical performance parameters of PDs were tested and analyzed. As shown in Fig. 3(b), the TPV test results indicate that the carrier recombination lifetime (2.30 μs) of the DBM-perovskite PDs is longer than that of the pristine PDs (1.62 μs), indicating reduced carrier recombination after introducing the DBM. As shown in Fig. 3(c), under zero bias, the J_d of the DBM-perovskite PDs is 7.31×10^{-8} mA·cm^{-2}, whereas that of the pristine PDs is 6.38×10^{-6} mA·cm^{-2}. The significant reduction in J_d is ascribed to the decreased defects in the DBM-perovskite film and the suppression of carrier recombination. Moreover, the DBM-perovskite PDs exhibit a significantly higher photocurrent at a representative wavelength of 980 nm than the pristine one, indicating efficient carrier transport[32]. Fig. S10 shows the current density we tested at wavelengths of 808 nm and 1 064 nm. The external quantum efficiency (EQE) of the fabricated PDs is exhibited in Fig. 3(d). Notably, the DBM-perovskite PDs exhibit an impressive EQE response in the wavelength range of 300-1 000 nm without external bias, which is significantly higher than the counterpart of the pristine PDs[33]. The

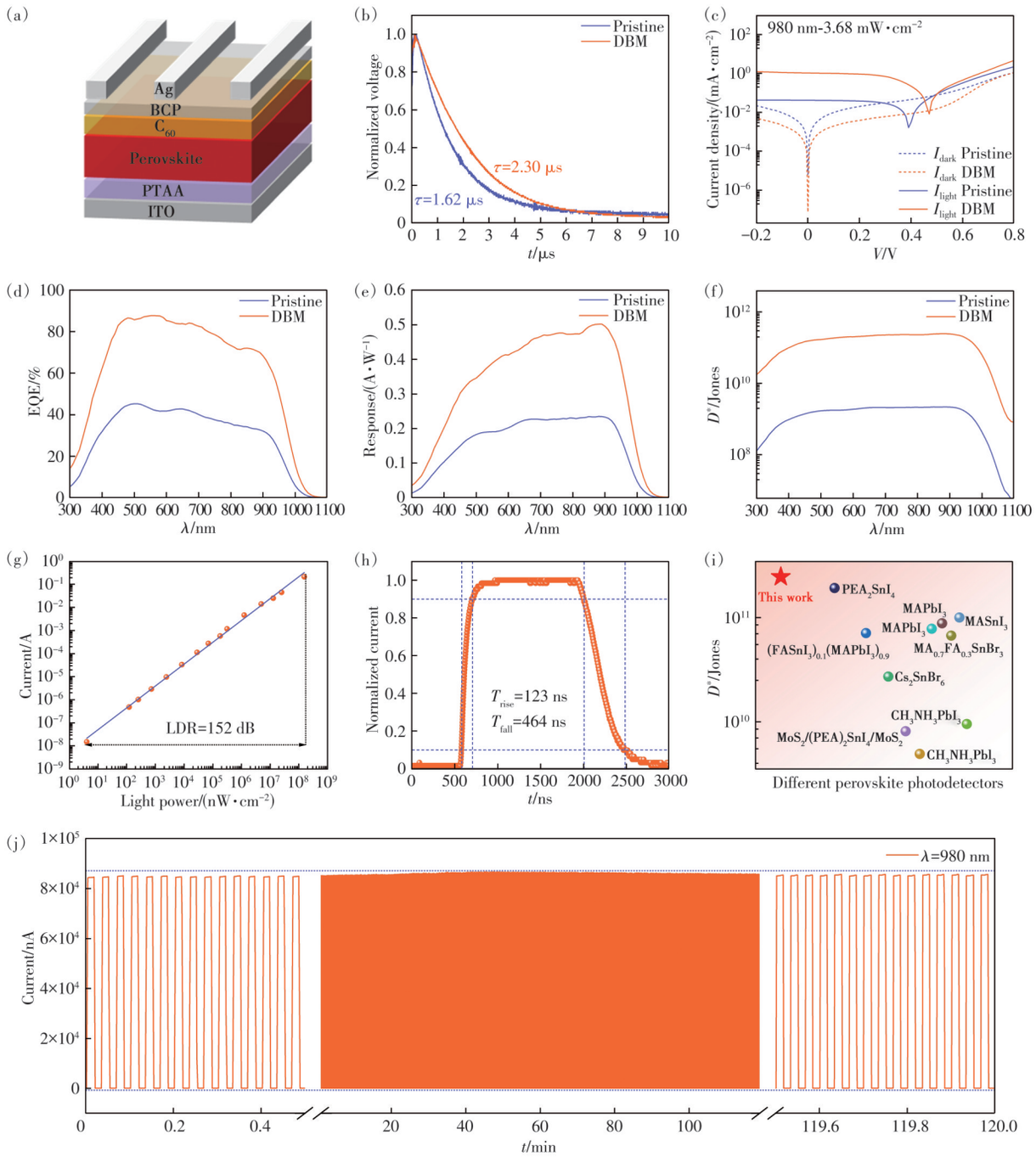

Fig. 3　(a) Structure diagram of the PDs. (b) TPV curves of the PDs with different perovskite films. (c) Current density-voltage characteristics of the fabricated PDs under dark and 980 nm illumination. EQE(d), R(e), D^*(f) of the PDs at zero bias. LDR(g), transient response(h) of the DBM-perovskite PDs. (i) D^* of the representatively reported NIR PDs. (j) Continuous on/off performance tracking of the optimal PDs at the wavelength of 980 nm under zero bias for 120 min

excellent performance can be ascribed to the efficient carrier transport, photocurrent extraction, and suppressed carrier recombination resulting from the homogeneous and smooth surface morphology, improved crystallinity, and reduced trap density of the DBM-perovskite film. Subsequently, a comparative analysis of the built-in electric field was carried out *via* the Mott-Schottky curves in order to investigate the carrier transport mechanism in detail.

As depicted in Fig. S11, the DBM-perovskite PDs demonstrate a higher built-in potential than the pristine sample, which contributed to the efficient charge carrier separation and transport. The DBM-perovskite PDs exhibit an exceptional NIR

response, achieving a maximum R of 0.51 $A \cdot W^{-1}$ in the NIR region (780 – 1 100 nm) at zero bias (Fig. 3(e)). Furthermore, the noise current spectra of the fabricated devices are presented in Fig. S12. It can be observed that the total noise of the device modulated by DBM is conspicuously lower than that of the pristine device, which is advantageous for the D^* and dynamic range. As exhibited in Fig. 3(f), the DBM-perovskite PDs also demonstrate a higher peak D^* of 2.46×10^{11} Jones than the pristine PDs (2.17×10^9 Jones) at the wavelength of 880 nm[34]. As depicted in Fig. 3(g), the dynamic range of the fabricated DBM-perovskite photodetector reaches 152 dB. A wide dynamic range implies that the photodetector fabricated possesses the potential to detect weak light signals[35-36].

The response speed is regarded as one of the most critical parameters for PDs, and it is generally evaluated by the response time. The response time includes the rise and fall time, which are defined as the time necessary for the current to ascend from 10% to 90% (90% to 10%) of the maximum response current signal[37-39]. As shown in Fig. 3(h), the fabricated self-powered PDs achieve fast rise/fall time of 123/464 ns. Fig. S13 shows the response time with multiple cycles and the corresponding input signals, respectively. Fig. 3(i) reveals that our photodetector possesses a superior D^* value among the reported NIR photodetectors. The compared results are summarized in Tab. S2. To assess the operational stability of the optimized PDs, the on/off stability of the DBM-perovskite PDs without any encapsulation was measured in ambient air under the NIR irradiation for 120 min. As shown in Fig. 3(j), the photocurrent (λ = 980 nm, $P_{in} \approx 4.26$ $mW \cdot cm^{-2}$) and dark current of the PDs demonstrated negligible attenuation during the operational process with a relatively large on/off ratio over 10^4. In addition, it also exhibits a stable output under the irradiation of 808 nm and 1 064 nm, as shown in Fig. S14. These results suggest that the fabricated NIR PDs can be stably operated in the ambient environment, demonstrating significant potential for applications in smart optoelectronics[40-41].

To estimate the imaging ability of the manufactured PDs, we fabricated the 5 × 5 PDs array with a single-pixel size of 3 mm × 3 mm. Fig. 4(b)

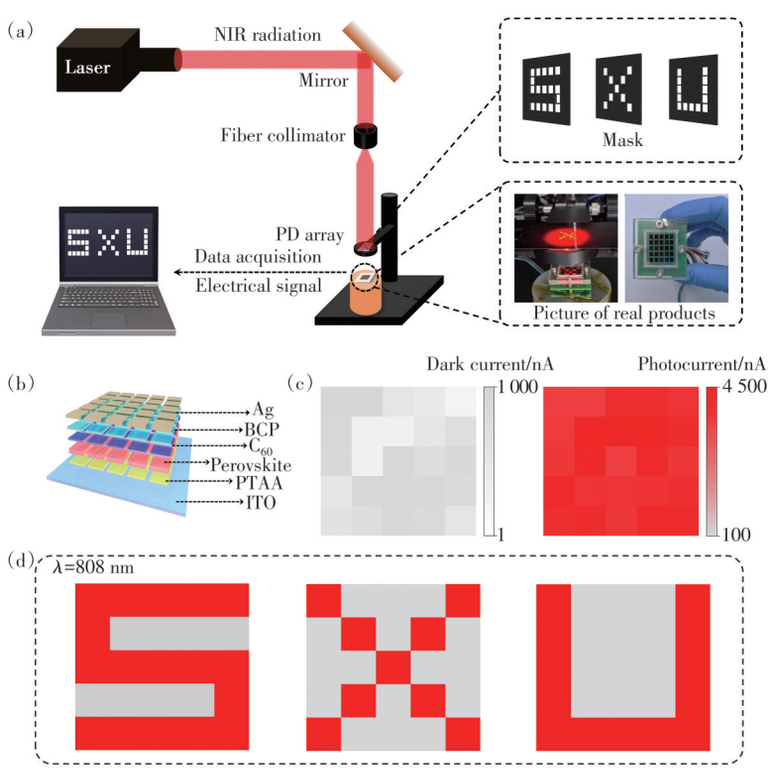

Fig. 4 (a)Schematic illustration of the NIR imaging system. (b)Structure of the PDs array. (c)The dark and photocurrent of the imaging array under the light of 808 nm, respectively. (d)Imaging of the 5 × 5 imaging array for the designed pattern with typical letters of "S", "X", and "U", operated at zero bias under 808 nm

illustrates the configuration of the imaging array. The imaging array and measurement system are shown in Fig. 4(a). NIR light was operated onto the imaging PDs array through designed masks with letters of "S", "X" and "U". The detector array converted the received optical signals into electrical signals, which were subsequently collected by a digital source meter and transmitted to a computer for processing, eventually yielding clear images.

The uniformity of pixel points is a crucial parameter for assessing the performance of the imaging array. The dark current and photocurrent of each pixel in the imaging array are shown in Fig. 4(c), with no significant difference in values and good uniformity. Fig. 4(d) and Fig. S15 show the imaging results of "S", "X" and "U" with clear outlines under 808 nm, 980 nm and 1 064 nm NIR light without external bias, indicating that the Sn-Pb mixed perovskite PDs have great potential in imaging applications.

4 Conclusion

In conclusion, we introduced the multifunctional DBM molecules to effectively regulate the crystallization of perovskite films, passivating surface defects and retarding the oxidation of Sn^{2+} to Sn^{4+}. The high-quality perovskite film controlled by DBM molecules enabled the self-powered NIR Sn-Pb mixed perovskite detector to exhibit superior performance, characterized by ultralow J_d, ultrafast response speed, a wide LDR, and excellent environmental stability. The fabricated PDs demonstrate a broad spectral response exceeding 1 000 nm, a high D^* of 2.46×10^{11} Jones, a large LDR of 152 dB, and ultrafast rise/fall time of 123/464 ns. Finally, the 5 × 5 pixels imaging array based on the DBM-perovskite film demonstrates clear imaging results in the NIR region. This work presents an effective strategy for achieving ultrafast response and a broad dynamic range in perovskite PDs, thereby promoting the commercial application of Sn-Pb mixed perovskite NIR PDs.

Supplementary Information and Response Letter are available for this paper at: http://cjl.lightpublishing.cn/thesisDetails#10.37188/CJL.20250027

References:

[1] TANG Y J, JIN P, WANG Y, *et al.* Enabling low-drift flexible perovskite photodetectors by electrical modulation for wearable health monitoring and weak light imaging [J]. *Nat. Commun.*, 2023, 14(1): 4961.

[2] MIN L L, SUN H X, GUO L Q, *et al.* Frequency-selective perovskite photodetector for anti-interference optical communications [J]. *Nat. Commun.*, 2024, 15(1): 2066.

[3] LI L L, XU H, LI Z X, *et al.* CMOS-compatible tellurium/silicon ultra-fast near-infrared photodetector [J]. *Small*, 2023, 19(42): 2303114.

[4] GIELEN S, KAISER C, VERSTRAETEN F, *et al.* Intrinsic detectivity limits of organic near-infrared photodetectors [J]. *Adv. Mater.*, 2020, 32(47): 2003818.

[5] WANG Z W, YIN Z Z, YANG Z Y, *et al.* Research progress of self-powered photodetectors based on halide perovskites [J]. *Chem. Eng. J.*, 2024, 501: 157512.

[6] 姜岩, 高峰, 李林. 具有宽带-窄带双功能探测模式的光电探测器 [J]. 发光学报, 2024, 45(4): 621-629.
JIANG Y, GAO F, LI L. Photodetector with broadband-narrowband dual-function detection mode [J]. *Chin. J. Lumin.*, 2024, 45(4): 621-629. (in Chinese)

[7] HAN P, GENG Y J, GUO F Y, *et al.* Alkali metal ion passivation of lead-free perovskite film for high responsivity self-powered broadband photodetectors [J]. *Chem. Eng. J.*, 2024, 490: 151876.

[8] 卢孟涵, 宋宏伟, 陈聪. 钙钛矿基宽谱带光电探测器 [J]. 发光学报, 2024, 45(6): 876-893.
LU M H, SONG H W, CHEN C. Perovskite based broadband photodetector [J]. *Chin. J. Lumin.*, 2024, 45(6): 876-893. (in Chinese)

[9] WANG Y R, LIN R X, WANG X Y, *et al.* Oxidation-resistant all-perovskite tandem solar cells in substrate configuration [J]. *Nat. Commun.*, 2023, 14(1): 1819.

[10] ZHU H L, CHOY W C H. Crystallization, properties, and challenges of low-bandgap Sn-Pb binary perovskites [J]. *Sol. RRL*, 2018, 2(10): 1800146.

[11] LIU L S, CAO F R, BIAN L K, *et al*. Ascorbic acid-induced porous iodide layer for a high-purity two-step solution-processed tin-lead mixed perovskite photodetector [J]. *J. Mater. Sci. Technol.*, 2025, 210: 227-232.

[12] GAO H, XIAO K, LIN R X, *et al*. Homogeneous crystallization and buried interface passivation for perovskite tandem solar modules [J]. *Science*, 2024, 383(6685): 855-859.

[13] LIANG H B, CHEN J, ZHU W J, *et al*. Synthesis of multifunctional organic molecules *via* Michael addition reaction to manage perovskite crystallization and defect [J]. *Angew. Chem.*, 2025, 137(1): e202413105.

[14] SU H, ZHANG J, HU Y J, *et al*. Modulation on electrostatic potential of passivator for highly efficient and stable perovskite solar cells [J]. *Adv. Funct. Mater.*, 2023, 33(34): 2213123.

[15] CHANG X Q, ZHONG J X, YANG G, *et al*. Targeted passivation and optimized interfacial carrier dynamics improving the efficiency and stability of hole transport layer-free narrow-bandgap perovskite solar cells [J]. *Sci. Bull.*, 2023, 68(12): 1271-1282.

[16] CHEN W T, SU K, HUANG Y Q, *et al*. Bifunctional additive 2-amino-3-hydroxypyridine for stable and high-efficiency tin-lead perovskite solar cells [J]. *J. Mater. Chem.* C, 2023, 11(1): 151-160.

[17] ZHAO W J, XU J, HE K, *et al*. A special additive enables all cations and anions passivation for stable perovskite solar cells with efficiency over 23% [J]. *Nano-Micro Lett.*, 2021, 13(1): 169.

[18] LIU H, WANG L X, LI R J, *et al*. Modulated crystallization and reduced V_{OC} deficit of mixed lead-tin perovskite solar cells with antioxidant caffeic acid [J]. *ACS Energy Lett.*, 2021, 6(8): 2907-2916.

[19] DUAN C H, ZOU F L, WEN Q Y, *et al*. A bifunctional carbazide additive for durable $CsSnI_3$ perovskite solar cells [J]. *Adv. Mater.*, 2023, 35(26): 2300503.

[20] ZHANG Z H, HUANG Y F, JIN J L, *et al*. Mechanistic understanding of oxidation of tin-based perovskite solar cells and mitigation strategies [J]. *Angew. Chem.*, 2023, 135(45): e202308093.

[21] LANZETTA L, WEBB T, ZIBOUCHE N, *et al*. Degradation mechanism of hybrid tin-based perovskite solar cells and the critical role of tin (IV) iodide [J]. *Nat. Commun.*, 2021, 12(1): 2853.

[22] LIU H, ZHU L, ZHANG H, *et al*. Realizing high-detectivity near-infrared photodetectors in tin-lead perovskites by double-sided surface-preferred distribution of multifunctional tin thiocyanate additive [J]. *ACS Energy Lett.*, 2022, 8(1): 577-589.

[23] HOSSAIN T, JOY S, DRAFFEN K, *et al*. Oxidation in tin halide perovskites: influence of acidic and basic additives [J]. *ACS Appl. Energy Mater.*, 2023, 6(24): 12334-12342.

[24] LIU B B, LI R, ZHUANG Q X, *et al*. Bottom-up holistic carrier management strategy induced synergistically by multiple chemical bonds to minimize energy losses for efficient and stable perovskite solar cells [J]. *J. Energy Chem.*, 2023, 76: 277-287.

[25] CHEN L, LI C W, XIAN Y M, *et al*. Incorporating potassium citrate to improve the performance of tin-lead perovskite solar cells [J]. *Adv. Energy Mater.*, 2023, 13(32): 2301218.

[26] ZHOU C, WANG F, AI X B, *et al*. Dual interfacial modification with 1D perovskite for self-assembled monolayer based inverted perovskite solar cells [J]. *Nano Energy*, 2024, 128: 109811.

[27] XIAO K, WEN J, HAN Q L, *et al*. Solution-processed monolithic all-perovskite triple-junction solar cells with efficiency exceeding 20% [J]. *ACS Energy Lett.*, 2020, 5(9): 2819-2826.

[28] LI Y Z, ZHANG Z B, ZHOU Y, *et al*. Enhanced performance and stability of ambient-processed $CH_3NH_3PbI_{3-x}(SCN)_x$ planar perovskite solar cells by introducing ammonium salts [J]. *Appl. Surf. Sci.*, 2020, 513: 145790.

[29] GUO T L, LIANG Z, LIU B Y, *et al*. Designing surface passivators through intramolecular potential manipulation for efficient and stable perovskite solar cells [J]. *Small*, 2024, 20(36): 2402197.

[30] LI F M, WU D, SHANG L, *et al*. Highly efficient monolithic perovskite/perovskite/silicon triple-junction solar cells [J]. *Adv. Mater.*, 2024, 36(16): 2311595.

[31] GAO C C, JIANG Y Z, SUN C J, *et al*. Multifunctional naphthol sulfonic salt incorporated in lead-free 2D tin halide perovskite for red light-emitting diodes [J]. *ACS Photonics*, 2020, 7(8): 1915-1922.

[32] XU X B, CHUEH C C, JING P F, *et al*. High-performance near-IR photodetector using low-bandgap $MA_{0.5}FA_{0.5}Pb_{0.5}Sn_{0.5}I_3$

perovskite [J]. *Adv. Funct. Mater.*, 2017, 27(28): 1701053.

[33] WEI H T, FANG Y J, YUAN Y B, *et al.* Trap engineering of CdTe nanoparticle for high gain, fast response, and low noise P3HT:CdTe nanocomposite photodetectors [J]. *Adv. Mater.*, 2015, 27(34): 4975-4981.

[34] SUN T, CHEN T, CHEN J H, *et al.* High-performance p-i-n perovskite photodetectors and image sensors with long-term operational stability enabled by a corrosion-resistant titanium nitride back electrode [J]. *Nanoscale*, 2023, 15(17): 7803-7811.

[35] LI C L, WANG H L, WANG F, *et al.* Ultrafast and broadband photodetectors based on a perovskite/organic bulk heterojunction for large-dynamic-range imaging [J]. *Light Sci. Appl.*, 2020, 9(1): 31.

[36] VUONG V H, PAMMI S V N, IPPILI S, *et al.* Flexible, stable, and self-powered photodetectors embedded with chemical vapor deposited lead-free bismuth mixed halide perovskite films [J]. *Chem. Eng. J.*, 2023, 458: 141473.

[37] ZHANG S W, LI Z L, LI J Z, *et al.* Organic near-infrared photodetectors with photoconductivity-enhanced performance [J]. *Aggregate*, 2023, 4(5): e345.

[38] QIAO S, LIU Y, LIU J H, *et al.* High-responsivity, fast, and self-powered narrowband perovskite heterojunction photodetectors with a tunable response range in the visible and near-infrared region [J]. *ACS Appl. Mater. Interfaces*, 2021, 13(29): 34625-34636.

[39] SARAN R, CURRY R J. Lead sulphide nanocrystal photodetector technologies [J]. *Nat. Photonics*, 2016, 10(2): 81-92.

[40] LIU M Y, LI Y C, YAO X, *et al.* A highly sensitive self-powered photodetector based on pinhole-free $PEA_{0.2}FA_{0.8}SnI_3$ films with aminopyrimidine [J]. *J. Mater. Chem.* A, 2024, 12(11): 6446-6454.

[41] BAO C X, XU W D, YANG J, *et al.* Bidirectional optical signal transmission between two identical devices using perovskite diodes [J]. *Nat. Electron.*, 2020, 3(3): 156-164.

刘晶晶(1997–),女,山西吕梁人,硕士研究生,2021年于太原师范学院获得学士学位,主要从事近红外光电探测与成像的研究。

E-mail: 202222607035@email.sxu.edu.cn

秦成兵(1986–),男,安徽六安人,博士,教授,博士生导师,2013年于中国科学技术大学获得博士学位,主要从事红外探测与成像的研究。

E-mail: chbqin@sxu.edu.cn

杨志春(1988–),男,山西朔州人,博士,副教授,硕士生导师,2021年于华中科技大学获得博士学位,主要从事光电转换材料与器件的研究。

E-mail: yangzhichun@sxu.edu.cn

肖连团(1966–),男,山西大同人,博士,教授,博士生导师,2001年于山西大学获得博士学位,主要从事激光光谱学和光子探测与成像的研究。

E-mail: xlt@sxu.edu.cn